ELSEVIER

Chemical Engineering Journal 122 (2006) 1–10

Chemical Engineering Journal

www.elsevier.com/locate/cej

Bubble size distribution and gas–liquid interfacial area in a modified downflow bubble column

Subrata Kumar Majumder*, Gautam Kundu, Dibyendu Mukherjee

Department of Chemical Engineering, Indian Institute of Technology, Kharagpur 721302, West Bengal, India

Received 6 January 2006; received in revised form 14 April 2006; accepted 19 April 2006

Abstract

Bubble size distribution and the gas–liquid specific interfacial area were measured as a function of axial location, nozzle diameter and superficial liquid and gas velocities in a modified bubble column reactor. The experimental measurements of bubble size and its distribution are analyzed with distribution model to gain insight into the breakup and coalescence mechanisms taking place. Axial profile of bubble number flux was estimated based on size distribution model incorporated with coalescence phenomena. Also correlation for Sauter mean bubble diameter has been developed with operating variables.

Keywords: Bubble size distribution; Interfacial area; Downflow bubble column; Gas–liquid dispersion

1. Introduction

Gas–liquid mass transfer is a crucial factor in the design of chemical and biochemical processes where dispersed phase is a reaction-limiting factor. Often the gas–liquid mass transfer is empirically determined from the time profile of concentration of dispersed phase in the system where information about bubble size and its distribution and interfacial area are neglected. However, a number of evidences have emphasized the significance of bubble properties in controlling the mass transfer in gas–liquid contacting systems. In general, the gas–liquid interfacial area is a function of unit's geometric size, operating parameters, physical and chemical properties of phases. In the case of absorption accompanied by slow or instantaneous reaction, mass transfer rate is determined by volumetric mass transfer coefficient, which is a function of specific interfacial area. So to optimize the processes on the mass transfer phenomena, it is essential to know the bubble size distribution and interfacial phenomena in the particular system at different operating conditions.

Several authors studied the bubble size and interfacial phenomena in different types of bubble column reactors. Colella et al. [1] studied the interfacial mechanisms focusing on the coalescence and breakage phenomena of bubbles in three different bubble columns. They investigated the influences of gas superficial velocity and different hydrodynamic configurations on bubble size distribution in the bubble columns. Lehr and Mewes [2] evaluated the bubble sizes in two-phase flow. They predicted the bubble size distribution in bubble columns including the formation of large bubbles at high superficial gas velocities. Schäfer et al. [3] discussed the influence of operating conditions and physical properties of gas and liquid phase on initial and stable bubble sizes in a bubble column reactor under industrial conditions. In recent years studies on bubble characteristics in ejector or venturi type bubble column are increasing as they offer distinct advantages over other conventional bubble columns in their ability to generate fine bubbles and a high gas–liquid interfacial transfer area. Dutta and Raghavan [4] investigated the mass transfer and hydrodynamic characteristics of a loop reactor using downflow liquid jet ejectors fitted with straight- and venturi-type throats. Cramers et al. [5] investigated the hydrodynamics and mass transfer characteristics of a loop-venturi reactor using a downflow liquid jet ejector. They determined the specific interfacial area of the ejector and the main holding vessel separately. Genenger and Lohrengel [6] developed a fully automatic measuring device to determine the bubble size distribution in a jet-driven loop reactor. Evans et al. [7] investigated the flow characteristics in the pipe-flow zone of a plunging liquid jet bubble column. Majumder et al. [8] studied the mixing characteristics and the dispersion coefficient of bubble motion in the ejector induced downflow bubble column reactor.

* Corresponding author.
E-mail address: rsmaju@yahoo.com (S.K. Majumder).

1385-8947/$ – see front matter © 2006 Elsevier B.V. All rights reserved.
doi:10.1016/j.cej.2006.04.007

Nomenclature

a	specific interfacial area (m^{-1})
A,B,C	axial locations defined along axial length as Z = 0.2–0.4 m, 0.4–0.6 m and 0.8–1.0 m, respectively
b_1–b_5	parameter used in Eq. (19)
C_{vm}	virtual mass coefficient
d_b	bubble diameter (m)
$d_{b,e}$	equivalent bubble diameter defined in Eq. (1) (m)
$d_{b,exp}$	bubble diameter during experiment (m)
d_{bi}	bubble diameter at ith class (m)
$d_{b,max}$	maximum bubble diameter (m)
$d_{b,min}$	minimum bubble diameter (m)
$d_{b,st}$	bubble diameter at standard condition (m)
d_c	column diameter (m)
d_n	nozzle diameter (m)
d_{vs}	Sauter mean bubble diameter (m)
D_R	ratio of Sauter mean bubble diameter to nozzle diameter (d_{vs}/d_n)
$\dot{f}(Z)$	rate of collisions per unit volume (m^3 s)$^{-1}$
Fr_n	gas Froude number based on nozzle diameter ($d_n g/V_{sg}^2$)
H_i	distance between gas–liquid mixing height and the point at which bubble image was taken (m)
K	correction factor, used in Eq. (13)
n	bubble number density (m^{-3})
$\dot{N}$	axial bubble number flux (m^2 s)$^{-1}$
N_i	number of bubbles in ith class
P_c	probability that a collision between two bubbles result in a coalescence event
P_{exp}	pressure during experiment (N/m^2)
P_{st}	pressure at standard condition (N/m^2)
Q_g	volumetric flowrate of gas (m^3/s)
Q_l	volumetric liquid flowrate (m^3/s)
R^2	correlation coefficient
Re_{ln}	liquid Reynolds number based on nozzle diameter ($d_n V_{sl}\rho_l/\mu_l$) (m)
Re_m	gas–liquid mixture Reynolds number, defined in Eq. (9)
Su_{ln}	liquid Suratman number based on nozzle diameter ($d_n\sigma_l\rho_l/\mu_l^2$)
t_d	drainage time (s)
t_i	interaction time (s)
t_p	persistence time (s)
T_{exp}	temperature during experiment (K)
u_0	relative velocity of the two bubbles at the onset of deformation (m/s)
u_*	friction velocity, defined in Eq. (8) (m/s)
V_j	jet velocity (m/s)
V_R	dispersed volume of reactor (m^3)
V_{sl},	superficial liquid velocity used in Eq. (8) (m/s)
V_{sg},	superficial gas velocity used in Eq. (8) (m/s)
V_{SR}	ratio of superficial gas velocity to superficial liquid velocity
V_t	turbulent velocity, defined in Eq. (6) (m/s)
Z	axial distance (m)
Z_R	ratio of axial length to nozzle diameter (Z/d_n)

Greek letters

$\bar{\epsilon}$	average energy dissipation rate per unit volume (kg/ms^3)
ε_g	fractional gas holdup
λ	constant of proportionality, used in Eq. (13)
μ_l	viscosity of liquid (kg/m s)
ρ_l	density of liquid (kg/m^3)
σ_l	surface tension of liquid (N/m)
ϕ_l	constant of proportionality used in Eq. (19)
ψ_l	functions, used in Eq. (17)

From the literature it was found that studies regarding the bubble characteristics and interfacial area in jet venturi type bubble column reactor have increased but there is little literature available for the bubble characteristics and the interfacial area in ejector type downflow bubble column reactor. In the present work, the bubble size distribution and the interfacial area have been studied in the ejector induced modified downflow bubble column.

2. Experimental setup and technique

The schematic diagram of the modified bubble column is shown in Fig. 1. It consists of an ejector assembly, E, an extended pipeline contactor, P, a gas–liquid separator, SE, and other accessories like centrifugal pump (P_1, P_2), manometer port (M_1–M_9), control valves (V_1–V_5), solenoid valves (SV_1–SV_4), rotameters (R_L, R_G), circulating tank (T), different sizes of nozzles, etc. The ejector assembly and extended pipeline contactor were made of transparent perspex for visual observation of the flow and mixing patterns. The major dimensions of the bubble column are given in Table 1. The forcing nozzle is of the straight hole type. An extended pipeline contactor was provided below the ejector assembly (Fig. 1) for gas–liquid two-phase downflow. The lower end of the contactor projected 0.45 m into the separator. This arrangement enabled uniform movement of the two-phase downflow and easy separation of the bubbles from the main stream. The air–liquid separator was sufficiently large (0.41 m × 0.41 m × 0.86 m, mild steel vessel) to minimize the effect due to liquid going out of the separator or gas–liquid separation. By operating the valves V_1, V_3–V_5, the liquid level inside the separator was maintained. The nozzle, the ejector assembly and the contactor were perfectly aligned in a vertical position to obtain an axially symmetric jet. For a particular flow through the nozzle, when the jet plunges into a liquid in the column, secondary air is entrained and two-phase mixing takes place in the mixing zone. A level of liquid is maintained at a particular height by adjusting the pressure in the separator. When the system reached steady state, axial column pressure, ΔP, gas entrainment rate, Q_g, and liquid flowrate, Q_l were noted. The data were collected for different nozzles, different liquid flowrate and dif-

Table 1
Dimensions of the ejector-column assembly

Description	Dimension (m)	Description	Dimension (m)
Height of the suction chamber, h_s	0.05	Diameter of the column, d_c	0.05
Diameter of suction chamber, d_s	0.06	Diameter of gas inlet, d_i	0.01
Diameter of throat, d_t	0.019	Length of the column, L_c	1.60
Length of the throat, L_t	0.183	Diameter of the nozzle used, d_n	0.004, 0.005, 0.006, 0.007
Length of the diffuser, L_d	0.254		

ferent controlled gas flowrate. Experiments have been carried out with air–water system. The experiments were repeated to check the reproducibility of data.

2.1. Bubble size determination

In the present work, bubble size distribution of the two-phase mixture was obtained by photographic method. The photographs were taken by illuminating the flow with uniform, diffused white light and capturing the image with a digital camera. The digital photographs were processed and enhanced by using Image Processing Software [Image Pro-Plus 5.0 (Media Cybernetics)] that enabled to distinguish clearly the bubble boundaries. The images were taken at three axial positions for different operating conditions. The 2d picture shapes of the bubbles were approximated by spheroids (Polli et al. [9]) whose maximum and minimum axes were automatically computed by the software program used for image analysis. The third dimension was calculated with the assumption that the bubbles are symmetric around the minimum axes. From the known values of maximum

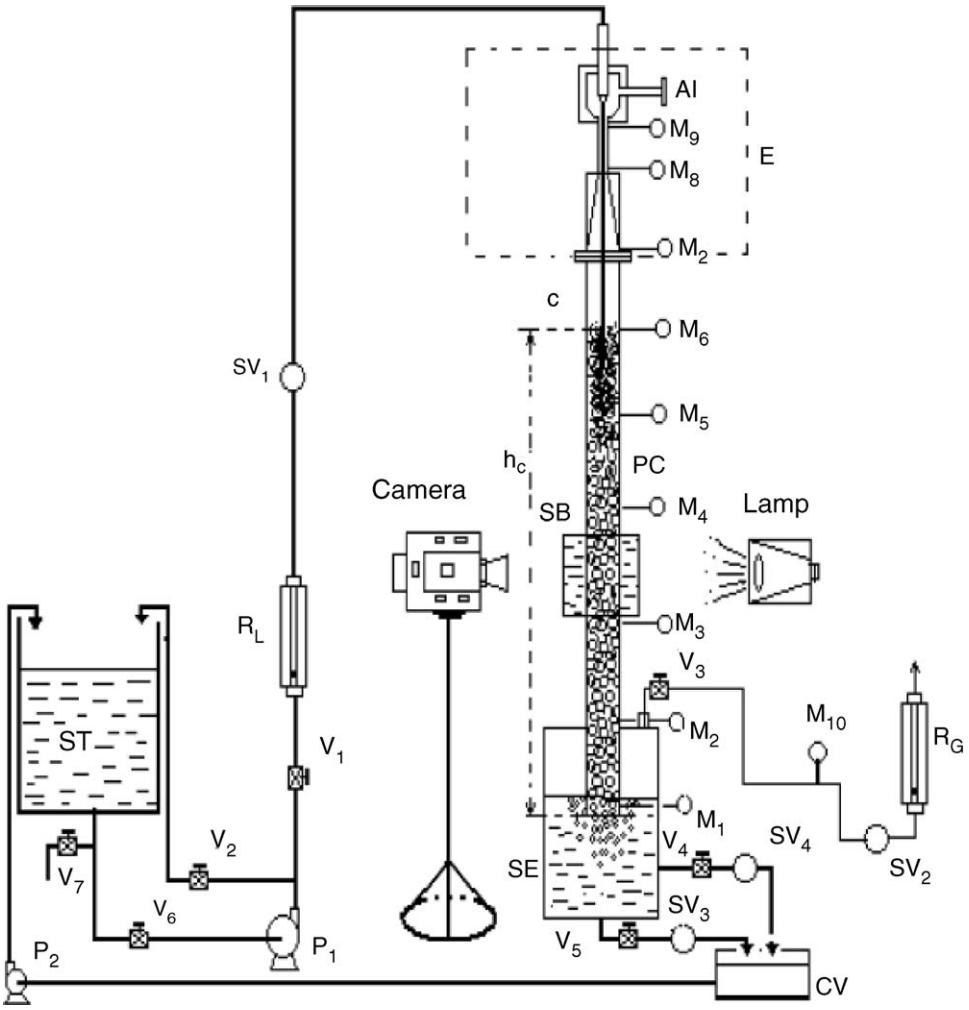

Fig. 1. Schematic diagram of experimental setup. *Legend*: AI: air inlet; CV: collector vessel; E: ejector assembly; C: level of gas–liquid mixture height; M_1–M_{10}: manometers; P_1 and P_2: pump; PC: pipeline contactor; R_L: rotameter for liquid; R_G: rotameter for gas; SB: water filled box; SE: separator; SV_1–SV_4: solenoid valves; ST: storage tank; TI: tracer inlet; V_1–V_7: valves.

Table 2
Discretization in bubble classes for axial location A at $d_n = 0.005$ m, $V_{sl} = 11.30 \times 10^{-2}$ m/s and $V_{sg} = 1.70 \times 10^{-3}$ m/s

Classes, i (mm)	Bubble number frequency in class i, N_i			Cumulative frequency in class i, $CF_i = \sum_1^i N_i$			Relative frequency, $N_i / \sum N_i$		
	Location			Location			Location		
	A	B	C	A	B	C	A	B	C
0–0.125	103	0	0	103	0	0	0.203	0	0
0.125–0.375	187	0	0	290	0	0	0.368	0	0
0.375–0.625	96	0	0	386	0	0	0.189	0	0
0.625–0.875	87	78	26	473	78	26	0.171	0.149	0.047
0.875–1.125	31	255	259	504	333	285	0.061	0.489	0.476
1.125–1.375	2	123	155	506	456	440	0.003	0.236	0.284
1.375–1.625	1	41	63	507	497	503	0.001	0.078	0.115
1.625–1.875	0	16	27	507	513	530	0	0.030	0.049
1.875–2.125	0	6	10	507	519	540	0	0.011	0.018
2.125–2.375	0	2	3	507	521	543	0	0.003	0.005
2.375–2.625	0	0	1	507	521	544	0	0	0.001
2.625–2.875	0	0	0	507	521	544	0	0	0
2.875–3.125	0	0	0	507	521	544	0	0	0
3.125–3.375	0	0	0	507	521	544	0	0	0

and minimum axes, an equivalent spherical bubble diameter was calculated by the following equation (Couvert et al. [10]):

$$d_{be} = \sqrt[3]{d_{b,max}^2 d_{b,min}} \quad (1)$$

where $d_{b,max}$ and $d_{b,min}$ are the maximum and minimum bubble diameter of bubble. The distributions were obtained by sorting the equivalent diameters of bubbles into different uniform classes. In Table 2 typical range of values for each class are shown in this study. For the consistency of the experiments, measurements were performed by taking four to seven pictures for each operating condition.

2.1.1. Error compensation in photographic technique

The photograph of bubble diameter in this study was taken in three axial locations. The radial distribution of bubble size was not observed as the column employed is of rather small cross-sectional area (column i.d.: 0.05 m). The measured sizes of bubbles may be subject to error by distortion due to curvature of the column surface. To overcome distortion problems due to the curvature of the pipe, a rectangular box (20 cm × 20 cm × 20 cm) filled with water (operating liquid) was used with a flat perspex window fitted on the perspex column (Fig. 2).

2.1.2. Pressure and temperature correction

The raw size of the bubble counted in a particular axial position is under the axial pressure and the room temperature. Therefore, corrections for pressure and temperature of the raw bubble size have to be made. Bubble size is reported at standard conditions [298 K and 1 atm] using the approximation given by following equations:

$$d_{b,st} = d_{b,exp} \sqrt[3]{\left(\frac{10.33 - H_i}{10.33}\right)\left(\frac{298}{T_i + 273}\right)} \quad (2)$$

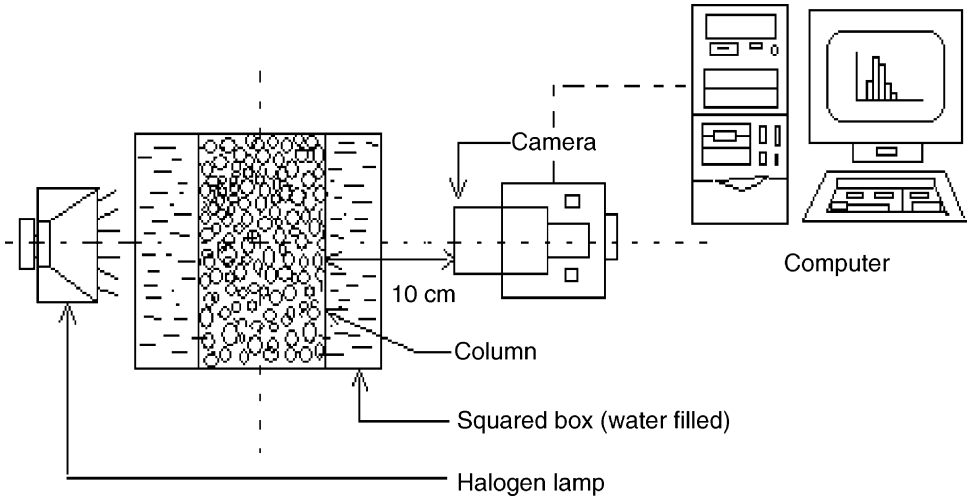

Fig. 2. Photographic arrangement.

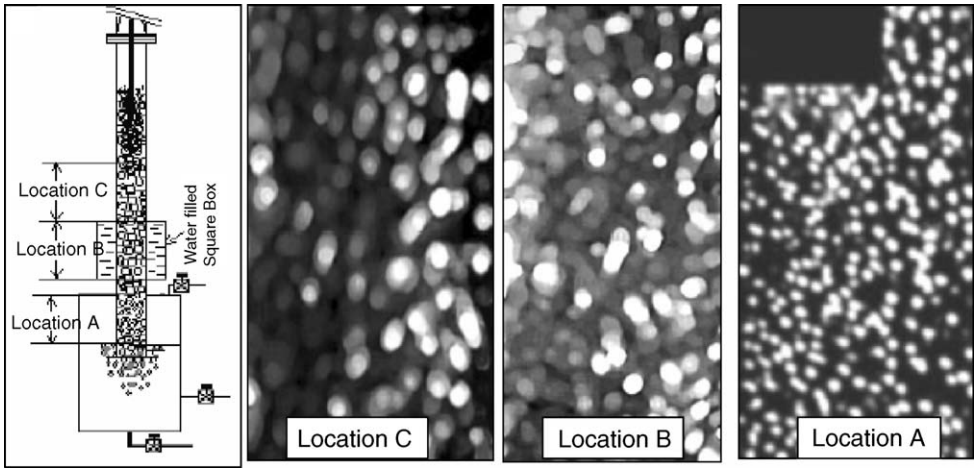

Fig. 3. Photograph taken from different location of homogeneous bubbly flow zone at $d_n = 0.005$ m, $V_{sl} = 7.07 \times 10^{-2}$ m/s and $V_{sg} = 1.70 \times 10^{-3}$ m/s.

where $d_{b,st}$ is the bubble diameter corrected to standard conditions, $d_{b,exp}$ the bubble diameter as taken from images, H_i the distance between the gas–liquid mixing height and the point at which the images are collected and T_i is the water temperature in the viewing chamber. All experiments were conducted at temperature $29 \pm 1\,^{\circ}$C.

At a particular operating condition, the bubble pictures taken from different locations of the column are shown in Fig. 3.

3. Bubble size distribution

It has been pointed out earlier that in the present system, gas–liquid mixing occurs in the extended contactor. The liquid jet after coming out from the divergent diffuser is arrested in the contactor by adjusting the liquid column height inside the column. When this jet impinges on the liquid surfaces inside the contactor, it entrains the surrounding gas along with it. The entrained gas undergoes subsequent breakdown and disintegrates as fine bubbles within a finite length, called intense mixing zone. In the intense mixing zone, the jet energy is utilized to form fine gas bubbles, which are carried downward by the bulk liquid motion and leave the mixing zone. The region below the mixing zone is referred to as homogeneous bubbly zone. The homogeneous bubbly flow zone consists of a relatively slow moving packed bed of bubbles. As the homogeneous bubbly flow zone consists of a relatively slow moving packed bed of bubbles, there is a probability of occurrence of coalescence between bubbles (Oolman and Blanch [11]). From the literature it is seen that models of bubble size distributions in swarms have been developed based on either (i) a binary coalescence process, whereby each coalescence event decreases the number of bubbles by one, or (ii) a non-binary process, which is based on simultaneous coalescence of bubble clusters. Stewart et al. [12] suggested that the binary model is adequate for predicting the bubble size distribution for systems in which coalescence does not occur. However, it is inappropriate for more routinely observed coalescing systems. In the following section the coalescence phenomena in the homogeneous bubbly flow zone has been emphasized from the size distribution model.

3.1. Model for size distribution

The size distribution model can be written based on a bubble number flux, $\dot{N}(Z)$. The balance for the bubble number flux over a volume element inside the column can be represented as follows (Atkinson et al. [13]):

$$\dot{N}(Z_2) = \dot{N}(Z_1) - \int_{Z_1}^{Z_2} P_c \dot{f}(Z)\,dZ \tag{3}$$

where $\dot{f}(Z)$ is the rate of collision per unit volume and P_c is the probability that a collision between two bubbles will result in a coalescence event. The collision frequency of bubbles can be found from statistical considerations analogous to the kinetic theory of gases in turbulent motions in the inertial subrange (Kamp et al. [14]). The number of collisions per unit time and volume of equal size bubbles is given by (Kuboi et al. [15]):

$$\dot{f}(Z) = \left(\frac{8\pi}{3}\right)^{0.5} n^2 d_b^2 V_t \tag{4}$$

where n is the bubble number density, which for spherical bubbles is equal to

$$n = \frac{6\bar{\varepsilon}_g}{\pi d_b^3} \tag{5}$$

and V_t is the turbulent velocity, which can be written as (Hinze [16])

$$V_t = \left(\frac{\bar{\in} d_b}{\rho_l}\right)^{1/3} \tag{6}$$

where $\bar{\in}$ is the average energy dissipation rate per unit volume in the homogeneous bubbly zone. According to Kamp et al. [14], the rate of energy dissipation of turbulent kinetic energy per unit volume in the bubbly flow zone can be estimated by the following equation:

$$\bar{\in} = \frac{2\rho_l u_*^3}{\kappa d_c} \tag{7}$$

where κ is the von Karman constant, equal to 0.41, and u_* is the friction velocity. The friction velocity can be estimated from Blasius equation (Colin et al. [17]) for the bubbly pipe-flow as follows:

$$u_* = (V_{sl} + V_{sg})\sqrt{\frac{0.079 Re_m^{-1/4}}{2}} \quad (8)$$

where Re_m is the gas–liquid mixture Reynolds number which is defined as

$$Re_m = \frac{\rho_l (V_{sl} + V_{sg}) d_c}{\mu_l} \quad (9)$$

Eqs. (3)–(9) can be used to predict the axial bubble number flux in the ejector induced downflow bubble column provided the probability of coalescence, P_c, is known. According to coalescence theory (Chesters [18]), coalescence occurs due to collision of two bubbles provided that the interaction time, t_i, between bubbles exceeds the drainage time, t_d. The drainage time is defined as the time required for drainage of the liquid film between bubbles to a critical rupture thickness. Kamp et al. [14] developed an explicit expression involving an exponential function for the probability of coalescence in terms of the ratio of the drainage, t_d, and interaction, t_i, times for two bubbles as

$$P_c \propto \exp\left(-\frac{t_d}{t_i}\right) \quad (10)$$

where

$$\frac{t_d}{t_i} = k\frac{\rho_l u_0 d^2/8\sigma}{\pi/4(\rho_l C_{vm} d^3/3\sigma)^{1/2}} \quad (11)$$

In Eq. (11), u_0 is the relative velocity of the two bubbles at the onset of deformation and C_{vm} is the virtual mass coefficient normally taken to be a value of 0.785 for spherical equal sized bubble diameter (Kamp et al. [14]). The parameter, k, in Eq. (11) is a correction factor, which is a function of bubble size and interfacial properties, to take into account hydrodynamic effects such as bubbles bouncing of each other prior to coalescence occurring. But the main limitation with Eq. (10) is that the mathematical definition for t_d does not include the effect of surface tension, which can change the drainage time by orders of magnitude. To some degree, the constant K, in Eq. (10), can be used to account for such effects. According to Atkinson et al. [13], the drainage time in Eq. (10) can be replaced with a constant, K times the bubble persistence time, t_p. The bubble persistence time is defined as the period that a rising bubble remains at the free surface before rupturing. It is a function of bubble size and liquid composition. Atkinson et al. [13] developed a correlation for the persistence time with air–water system and obtained as

$$t_p = 2.60 \times 10^7 d_b^{3.02} \quad (12)$$

Therefore, Eq. (10) can be written as

$$P_c = \lambda \exp\left(-\frac{K t_p}{t_i}\right) \quad (13)$$

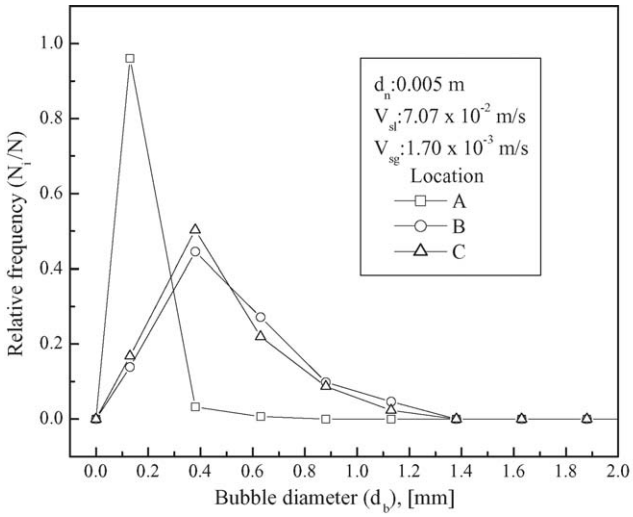

Fig. 4. Bubble size distribution at different locations.

where λ is the constant of proportionality. The probability of coalescence is determined by calculating the persistence and interaction times from Eqs. (12) and (11), respectively. λ and K are unknown parameters, to be adjusted to obtain a best fit for the bubble number flux $[\dot{N}(Z)]$ over a volume element inside the column calculated in accordance with Eq. (3). The profile of the bubble flux, $\dot{N}(Z)$, in the bubbly low zone was calculated based on the gas volumetric flowrate, Q_g, column cross-sectional area, A_c, and the measured Sauter mean bubble diameter, d_{vs}. The profile for the bubble number flux is represented by:

$$\dot{N}(Z) = \frac{\text{Gas volumetric flowrate}}{\text{Bubble volume} \times \text{Cross-sectional area}} = \frac{Q_g}{\pi/6 d_{vs}^3 \times \pi/4 d_c^2} = \frac{24 Q_g}{d_{vs}^3 \times d_c^2} \quad (14)$$

4. Results and discussion

4.1. Bubble size distribution

4.1.1. Effects of operating variables on bubble size distribution

The bubble size distribution was obtained in three axial locations A (of height 0.2–0.4 m), B (of height 0.4–0.6 m) and C (of height 0.8–1.0 m) from the bottom of the column (Fig. 3). Typical results for these three locations are presented in Figs. 4 and 5. It is seen that the bubble sizes in locations B and C are greater than location A (Fig. 4). The average bubble size in locations B and C are almost same. In the intense mixing zone, high rate of energy dissipation results in the generation of bubbles. Larger bubbles generated in the mixing zone are broken up into fine bubbles by the momentum of the liquid jet and carried downward by the bulk liquid motion and distributed along the axis. The distribution of the bubble size occurs according to axial energy dissipation profile (Evans et al. [7]). In all cases, the bubble size distribution was not symmetrical (normal distribution) with an extended tail for the larger bubble sizes, which is typical of a lognormal distribution. Fig. 6 shows the typical well

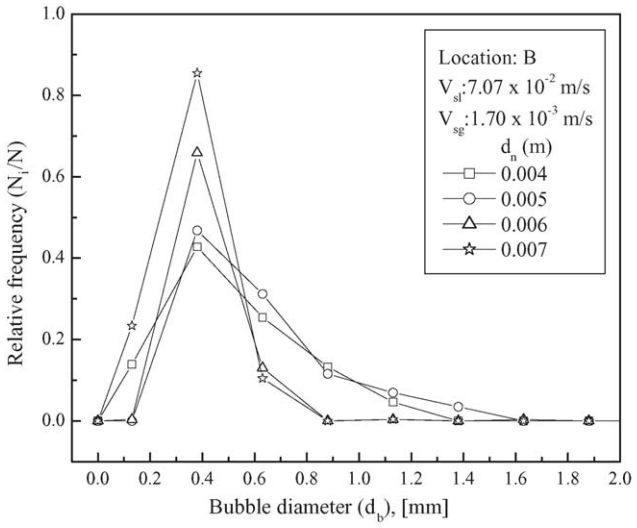

Fig. 5. Bubble size distribution at different nozzle diameters.

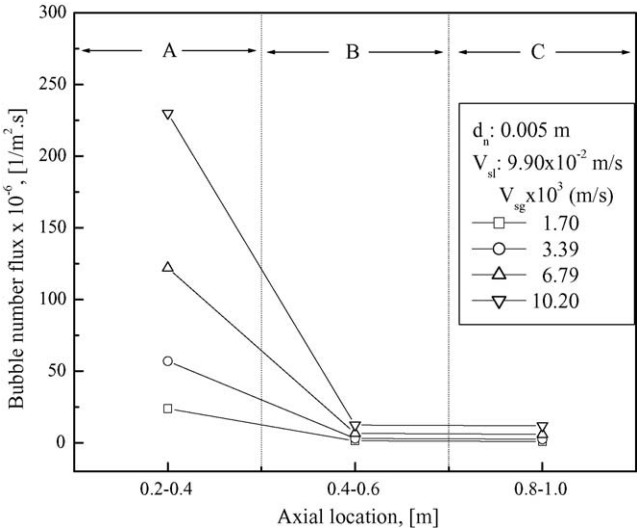

Fig. 7. Variation of bubble number flux with axial location at different superficial gas velocities.

fitted lognormal distribution compared with other distributions for a particular operating condition. All calculations regarding goodness of fit have been performed by STAT::FIT software. Bubble diameter increased with increasing distance from the bottom of the column due to the coalescence of smaller bubbles. The coalesced bubbles of location A go up due to their buoyancy and accumulate in the location B and C. This results in the wider bubble size distribution in locations B and C compared to location A. Also the bubble number flux varies in different locations due to the same reason. Typical profiles of bubble number flux are shown in Fig. 7. That bubble number flux decreases in locations B and C over location A is the result of an increase in bubble size due to coalescence. The probability of coalescence (P_c) depends on bubble–bubble interaction time (t_i) and bubble persistence time (t_p). The calculated value of probability of coalescence is 0.000664, which indicates that the probability of coalescence when two bubbles collide is very low. The calculated probability corresponded to a persistence and interaction time of 0.0012 and 0.00035 s, respectively (Eq. (13)). The probability of coalescence increases with the increase in liquid flowrate as shown in Fig. 8. This is because of increasing collision frequency between bubbles with increase in liquid flowrate. As the liquid flowrate increases, kinetic energy increases, which increase the turbulence intensity, bubble–bubble interaction and velocity of bubbles. It is also seen from Fig. 8 that the probability of coalescence is higher in region A than other regions. In the region A at a particular liquid flowrate the persistence time t_p decreases as the bubble size decreases (Eq. (12)) which causes the relatively higher probability of coalescence in region.

4.2. Specific interfacial area and Sauter mean bubble diameter

The interfacial area is one of the most important parameters for gas–liquid reactor design. Experimental methods for

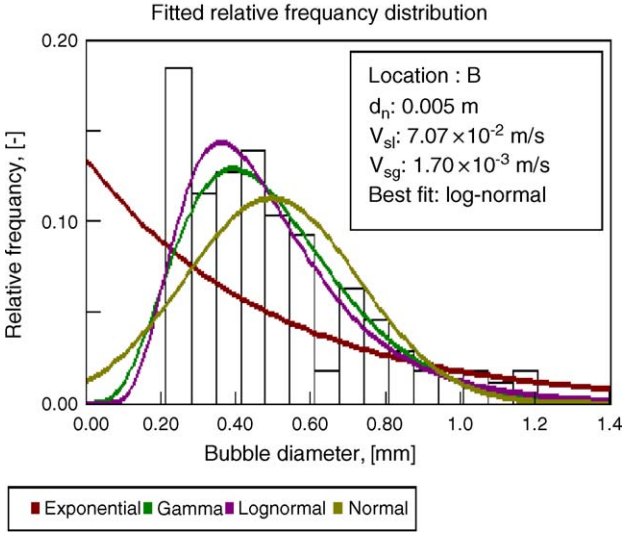

Fig. 6. Fitted different distributions of bubble sizes at location B.

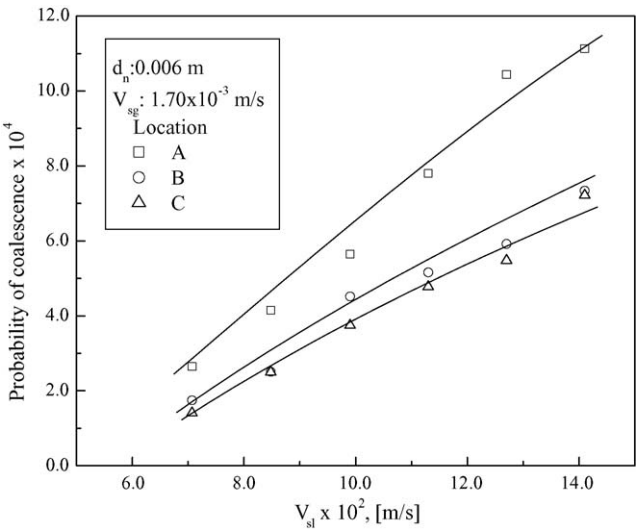

Fig. 8. Variation of probability of coalescence with superficial liquid velocity.

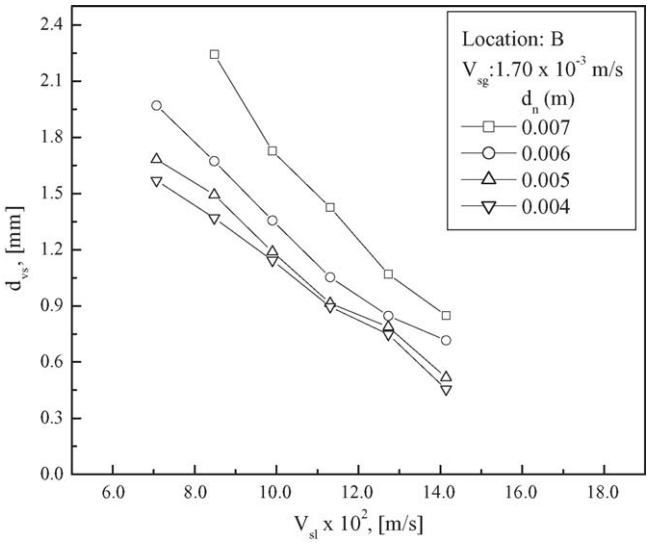

Fig. 9. Effect of superficial liquid velocity on Sauter mean bubble diameter for different nozzle diameters.

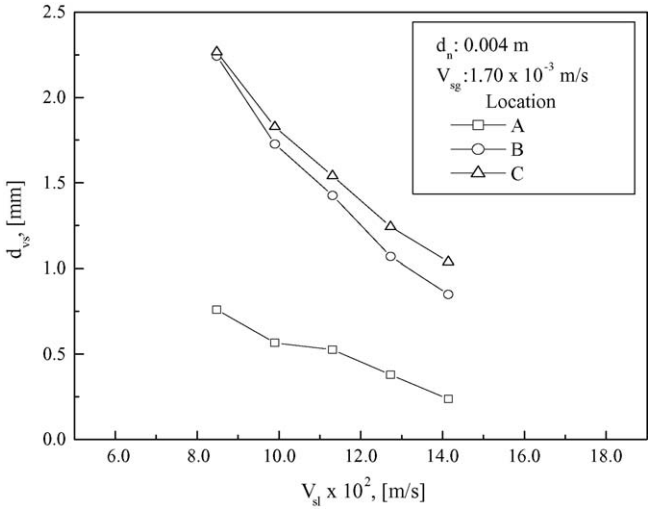

Fig. 10. Effect of superficial liquid velocity on Sauter mean bubble diameter in different locations.

determining interfacial area in bubble columns can be divided into two groups, one being physical and other chemical. Physical measuring processes give local values of interfacial area, whereas the whole reactor volume can be assessed by using chemical methods (Deckwer [19]). In this present study specific interfacial area was determined by physical method based on the bubble size distribution. Provided the gas holdup (ε_g) is known, specific interfacial area (a) can be calculated from the following equation:

$$a = \frac{6\varepsilon_g}{d_{vs}} \tag{15}$$

The Sauter mean bubble diameter (d_{vs}) is defined as the volume-to-surface mean bubble diameter:

$$d_{vs} = \frac{\sum_{i=1}^{N}(N_i d_{bi}^3)}{\sum_{i=1}^{N}(N_i d_{bi}^2)} \tag{16}$$

where N_i is the number of bubbles of diameter d_{bi}.

4.2.1. Effects of operating variables on Sauter mean bubble diameter and specific interfacial area

The Sauter mean bubble diameters in three different axial positions were investigated with different nozzle diameters. Tests were conducted at superficial liquid velocity 7.07×10^{-2}–14.14×10^{-2} m/s and superficial gas velocity 1.70×10^{-3}–13.58×10^{-3} m/s. Typical profiles of the Sauter mean diameter (d_{vs}) as a function of superficial liquid velocity for different nozzle diameters and for different locations are shown in Figs. 9 and 10, respectively. The bubble size decreases with increasing superficial liquid velocity in each location. This is due to bubble break up with increasing momentum transfer of liquid jet with increasing liquid flowrate. As shown in Fig. 10, there is no significant variation of bubble size in locations B and C, whereas the bubble in location A is much smaller than the location B and C. It may be seen from Fig. 9 that bubble size increases with increasing nozzle diameter. This is expected since the energy input to the mixing zone is inversely proportional to the square of the nozzle diameter ($E \propto V_j^2$ or $1/d_n^2$). At smaller nozzle diameter, relatively smaller bubbles are formed as the energy input is higher. It was observed that as the nozzle diameter decreases the bubble size decreases at locations B and C. This is due to more kinetic energy for smaller nozzle diameter. Also the rate of coalescence increases as the gas flowrate increases. As the gas flowrate increases the gas holdup increases which enhances bubble–bubble interactions. This results in increase in probability of coalescence with increase in superficial gas velocity. Also as the superficial gas velocity increases, the Sauter mean bubble diameter increases (Fig. 11). This may be due to less liquid resistance inside the column. The bubble size increases with the decrease of liquid resistance inside the column. The liquid resistance decreases as the superficial gas velocity increases due to increase of gas holdup with increase in superficial gas velocity. The specific interfacial area was calculated by Eq. (15). From

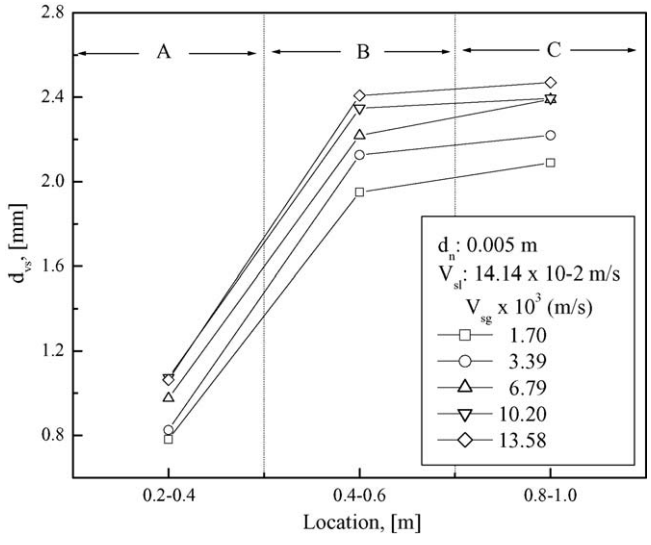

Fig. 11. Variation of Sauter mean bubble diameter with axial location.

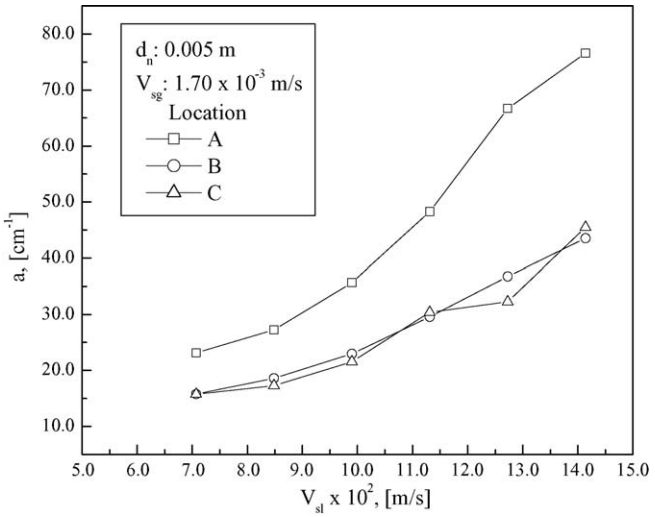

Fig. 12. Variation of specific interfacial area with superficial liquid velocity for different axial locations.

the experimental result it is seen that the specific interfacial area varies with the operating variables as well as the location of the column. The specific interfacial area is related to the Sauter mean bubble diameter and the gas holdup. As discussed earlier, the Sauter mean bubble diameter decreases and the gas holdup increases with the increase of both superficial liquid and gas velocities. Decrease of Sauter mean bubble diameter and the increase of gas holdup would result in the increase of specific interfacial area with liquid velocity (Fig. 12). A typical profile of local gas holdup is shown in Fig. 13. Also the specific interfacial area varies with the axial location. This is because of variation of the Sauter mean bubble diameter and gas holdup with the axial location. The Sauter mean bubble diameter varies with axial location due to coalescence effect whereas the variation of gas holdup is due to variation of bubble number flux as discussed earlier.

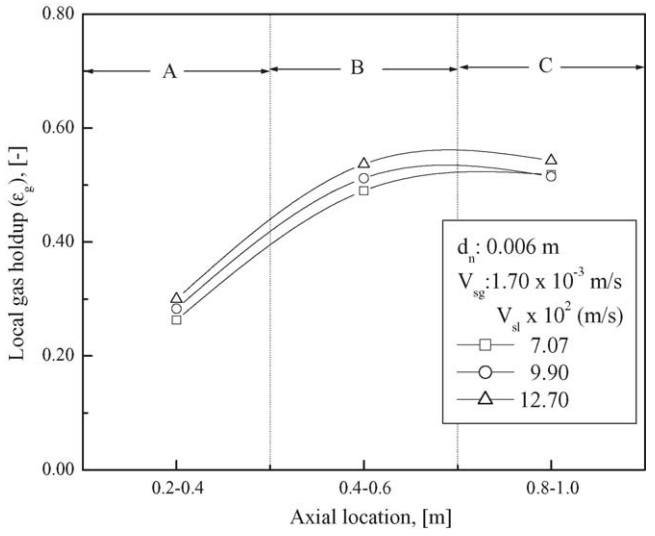

Fig. 13. Local gas holdup distribution at different superficial liquid velocities.

4.3. Prediction of bubble size

The formation of bubble by plunging liquid jet in a downflow column is very complex phenomena and there is no reliable theoretical model available to predict the bubble size in the plunging liquid jet bubble column. It is very difficult to develop a theoretical model to predict the bubble size for the present system due to the complexity of the system. In the present study an attempt has been made to predict bubble size by developing an empirical correlation. It has been found experimentally that bubble size depends on different operating variables: fluid flowrates, nozzle diameter and axial location in the column. Therefore, the correlation has been developed with the different operating variables. To develop the correlation, the experimental data has been analyzed by expressing Sauter mean bubble diameter as a function of the following parameters:

$$d_{vs} = \psi_1(V_{sl}, V_{sg}, d_n, Z, \rho_l, \mu_l, \sigma_l, g) \quad (17)$$

Applying Rayleigh's method of dimensional analysis, Eq. (17) can be represented with significant dimensionless groups as follows:

$$D_R = \psi_1(Z_R, V_R, Fr_n, Re_{ln}, Su_{ln}) \quad (18)$$

To develop a functional relationship between D_R and other dimensionless groups in Eq. (18), the functionality can be expressed as follows:

$$D_R = \phi_1 Z_R^{b1} V_{SR}^{b2} Fr_n^{b3} Re_{ln}^{b4} Su_{ln}^{b5} \quad (19)$$

The multiple linear regression analysis on 495 experimental data gives the following generalized correlation for air–water system;:

$$D_R = 1.48 \times 10^{-2} Z_R^{1.09} V_R^{-1.388} Fr_n^{-0759} Re_{ln}^{0.449} Su_{ln}^{-0.303} \quad (20)$$

The correlation coefficient and standard error of Eq. (20) were found to be 0.971 and 0.057, respectively. The ranges of variation

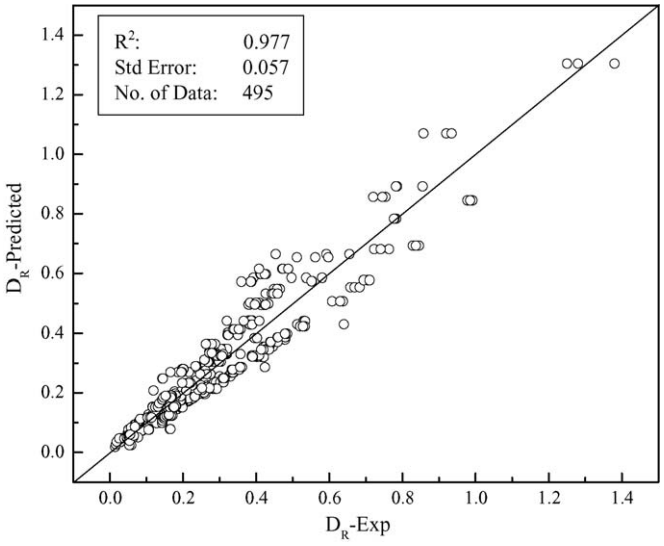

Fig. 14. Comparison between predicted and measured Sauter mean bubble diameter.

of the different parameters for the correlation are as follows:

$$42.85 < Z_R < 225.00;\ 8.23 \times 10^{-3} < V_{SR} < 174.55 \times 10^{-3};\ 0.02 \times 10^4 < Fr_n < 2.38 \times 10^4;\ 2.83 \times 10^2 < Re_{ln} < 17.97 \times 10^2;\ 4.45 \times 10^5 < Su_{ln} < 7.80 \times 10^5.$$

The calculated values of D_R were plotted against the experimental values and are shown in Fig. 14.

5. Conclusion

To understand the interfacial mechanisms of the present gas–liquid modified bubble column detailed sets of data on bubble size distribution were investigated. In order to obtain the distribution curves about 400–1000 bubbles were analyzed. The measurements were done using photographic technique. The evaluation of bubble size distribution in different locations of the column and the influence of nozzle diameter and superficial liquid and gas velocities were pointed out. The bubble size in the bubbly flow zone increased with increasing distance from the bottom of the column due to coalescence and kinetic energy distribution. The bubble size distribution for each axial position was best fitted to lognormal distribution, which was consistent with the other studies. The bubble number flux, as a function of axial position has been estimated based on the bubble number concentration, collision frequency of bubbles and the probability of coalescence taking place. Correlations have been developed to predict the bubble size, which agree well with the experimental results. The correlations may be recommended to scale-up the system for industrial applications.

Acknowledgement

The authors wish to acknowledge the Council of Scientific and Industrial Research, Human Resource Development Group, India, for financial support towards this research project.

References

[1] D. Colella, D. Vinci, R. Bagatin, M. Masi, E. Abu Bakr, A study on coalescence and breakage mechanisms in three different bubble columns, Chem. Eng. Sci. 54 (1999) 2331.

[2] F. Lehr, D. Mewes, A transport equation for the interfacial area density applied to bubble columns, Chem. Eng. Sci. 56 (February (3)) (2001) 1159–1166.

[3] R. Schäfer, C. Merten, G. Eigenberger, Bubble size distributions in a bubble column reactor under industrial conditions, Exp. Therm. Fluid Sci. 26 (August (6–7)) (2002) 595–604.

[4] N.N. Dutta, K.V. Raghavan, Mass transfer and hydrodynamics of loop reactors with downflow liquid jet ejector, Chem. Eng. J. 36 (1987) 111–121.

[5] P.H.M.R. Cramers, A.A.C.M. Beenackers, L.L. Van Dierendonck, Hydrodynamics and mass transfer characteristics of a loop-venturi reactor, Chem. Eng. Sci. 47 (1992) 3557–3564.

[6] B. Genenger, B. Lohrengel, Measuring device for gas/liquid flow, Chem. Eng. Process. 31 (May (2)) (1992) 87–96.

[7] G.M. Evans, G.J. Jameson, C.D. Rielly, Free jet expansion and gas entrainment characteristics of a plunging liquid jet, Exp. Therm. Fluid Sci. 12 (February (2)) (1996) 142–149.

[8] S.K. Majumder, G. Kundu, D. Mukherjee, Mixing mechanism in ejector induced downflow bubble column, Chem. Eng. J. 112 (1–3) (2005) 45–55.

[9] M. Polli, M.D. Stanislao, R. Bagatin, E. Abu Bakr, M. Masi, Bubble size distribution in the sparger region of bubble columns, Chem. Eng. Sci. 57 (January (1)) (2002) 197–205.

[10] A. Couvert, M. Roustan, P. Chatellier, Two-phase hydrodynamic study of a rectangular airlift loop reactor with an internal baffle, Chem. Eng. Sci. 54 (1999) 5245–5252.

[11] T.O. Oolman, H.W. Blanch, Bubble coalescence in air-sparged bioreactors, Biotechnol. Bioeng. 28 (1986) 578–584.

[12] C.W. Stewart, C.T. Crowe, S.C. Saunders, A model for simultaneous coalescence of bubble clusters, Chem. Eng. Sci. 48 (1993) 3347–3354.

[13] B.W. Atkinson, G.J. Jameson, A.V. Nguyen, G.M. Evans, P.M. Machniewski, Bubble breakup and coalescence in a plunging liquid jet bubble column, Can. J. Chem. Eng. 81 (June–August) (2003) 519–527.

[14] A.M. Kamp, A.K. Chesters, C. Colin, J. Fabre, Bubble coalescence in turbulent flows: a mechanistic model for turbulence-induced coalescence applied to microgravity bubbly pipe flow, Int. J. Multiphase Flow 27 (August (8)) (2001) 1363–1396.

[15] R. Kuboi, I. Komosawa, T. Otake, Collision and coalescence of dispersed drops in turbulent liquid flow, J. Chem. Eng. Jpn. 5 (1972) 423–424.

[16] J.O. Hinze, Turbulence—an introduction to its mechanism and theory, McGraw-Hill, New York, NY, 1975.

[17] C. Colin, J. Fabre, A. Dukler, Gas liquid flow at microgravity conditions—I (dispersed bubble and slug flow), Int. J. Multiphase Flow 17 (1991) 533–544.

[18] A.K. Chesters, The modeling of coalescence processes in fluid–fluid dispersions: a review of current understanding, Trans. Inst. Chem. Eng. 69 (1991) 259–270.

[19] W.D. Deckwer, Bubble Column Reactors, Wiley, New York, 1992.